

FIRST SYSTEMATIC SEARCH FOR OXYGEN-LINE BLOBS AT HIGH REDSHIFT: UNCOVERING AGN FEEDBACK AND STAR FORMATION QUENCHING

SURAPHONG YUMA¹, MASAMI OUCHI¹, ALYSSA B. DRAKE², CHRIS SIMPSON², KAZUHIRO SHIMASAKU³, KIMIHIKO NAKAJIMA³,
 YOSHIKI ONO¹, RIEKO MOMOSE¹, MASAYUKI AKIYAMA⁴, MASAO MORI⁵, AND MASAYUKI UMEMURA⁵

¹ Institute for Cosmic Ray Research, The University of Tokyo, Kashiwa-no-ha, Kashiwa 277-8582, Japan; yuma@icrr.u-tokyo.ac.jp

² Astrophysics Research Institute, Liverpool John Moores University, IC2, Liverpool Science Park, 146 Brownlow Hill, Liverpool L3 5RF, UK

³ Department of Astronomy, Graduate School of Science, The University of Tokyo, Hongo, Bunkyo-ku, Tokyo 113-0033, Japan

⁴ Astronomical Institute, Tohoku University, Aoba-ku, Sendai 980-8578, Japan

⁵ Center for Computational Science, University of Tsukuba, Tsukuba, Ibaraki 305-8577, Japan

Received 2013 June 21; accepted 2013 October 9; published 2013 November 25

ABSTRACT

We present the first *systematic* search for extended metal-line [O II] $\lambda\lambda 3726, 3729$ nebulae, or [O II] blobs (O II Bs), at $z = 1.2$ using deep narrowband imaging with a survey volume of $1.9 \times 10^5 \text{ Mpc}^3$ on the 0.62 deg^2 sky of Subaru-*XMM* Deep Survey (SXDS) field. We discover a giant O II B, called “O II B 1,” with a spatial extent over $\sim 75 \text{ kpc}$ at a spectroscopic redshift of $z = 1.18$, and also identify a total of 12 O II Bs with a size of $> 30 \text{ kpc}$. Our optical spectrum of O II B 1 presents [Ne V] $\lambda 3426$ line at the 6σ level, indicating that this object harbors an obscured type-2 active galactic nucleus (AGN). The presence of gas outflows in this object is suggested by two marginal detections of Fe II $\lambda 2587$ absorption and Fe II* $\lambda 2613$ emission lines both of which are blueshifted at as large as $500\text{--}600 \text{ km s}^{-1}$, indicating that the heating source of O II B 1 is AGN or associated shock excitation rather than supernovae produced by starbursts. The number density of O II B 1-type giant blobs is estimated to be $\sim 5 \times 10^{-6} \text{ Mpc}^{-3}$ at $z \sim 1.2$, which is comparable with that of AGNs driving outflow at a similar redshift, suggesting that giant O II Bs are produced only by AGN activity. On the other hand, the number density of small O II Bs, $6 \times 10^{-5} \text{ Mpc}^{-3}$, compared to that of $z \sim 1$ galaxies in the blue cloud in the same M_B range, may imply that 3% of star-forming galaxies at $z \sim 1$ are quenching star formation through outflows involving extended [O II] emission.

Key words: galaxy: evolution – galaxies: high-redshift

Online-only material: color figures

1. INTRODUCTION

Elliptical galaxies are one of the most common galaxy populations in the local universe. They are featureless and dominated by old stars with very low or zero star formation rates (SFRs). Their formation and evolution processes have been studied over decades both theoretically and observationally. Many simulations suggest that major mergers of two galaxies with comparable masses can produce giant elliptical galaxies (Toomre 1977; Barnes & Hernquist 1992; Naab & Trujillo 2006). Basically, the progenitors of elliptical galaxies have to stop forming new stars and begin evolving passively at some epoch in the past. That epoch should be as early as $z \gtrsim 1$, because the luminosity–size and stellar mass–size relations of early-type galaxies from $z \sim 1$ evolve consistently with completely passive evolution of their stellar populations (Trujillo & Aguerri 2004; McIntosh et al. 2005). It is not yet understood what makes galaxies stop forming stars and start to evolve passively. One popular proposed mechanism for quenching star formation is gas outflows by a starburst and/or an active galactic nucleus (AGN; e.g., Dekel et al. 2009). Therefore, studying outflow processes at $z \gtrsim 1$ (especially in massive galaxies) is of importance in understanding the evolution of quiescent elliptical galaxies.

Besides the quenching process of star formation activity, the gas outflow is also a crucial solution to various observational puzzles seen, e.g., in the mass–metallicity relation (e.g., Tremonti et al. 2004) and the chemical enrichment of the interstellar medium (ISM) and the intergalactic medium (IGM;

e.g., Martin 2005; Rupke et al. 2005a, 2005b; Weiner et al. 2009; Coil et al. 2011). Galactic outflows are theoretically the primary mechanism for regulating the baryon and metallicity abundances of galaxies. Without strong feedback, cosmological models of galaxy evolution produce too many galaxies with high SFRs and large stellar masses compared to observations (e.g., Cole et al. 2000; Springel & Hernquist 2003; Kereš et al. 2009). Some process is thus needed to prevent gas from cooling into the central galaxies of dark matter halos and forming stars. At the low-mass end of the galaxy mass function, feedback driven by supernovae (SNe) is often referred to as an energy/momentum input for outflowing gas from galaxies (Dekel & Silk 1986; Springel & Hernquist 2003; Murray et al. 2005). Meanwhile, models with feedback from AGN possibly account for the presence of massive elliptical galaxies (e.g., Somerville et al. 2008).

Observationally, galactic-scale outflows have been widely found in local ultra luminous infrared galaxies (ULIRGs; e.g., Heckman et al. 1990; Martin 2005; Soto et al. 2012), in post-starburst galaxies at $0.2 < z < 0.8$ (e.g., Coil et al. 2011), in radio galaxies at $z \sim 0.5$ (e.g., Nesvadba et al. 2008; Liu et al. 2013), in normal star-forming galaxies (e.g., Steidel et al. 2010; Martin et al. 2012; Kornei et al. 2012; Erb et al. 2012; Bradshaw et al. 2013), and in sub-millimeter galaxies at $z \sim 2$ (e.g., Alexander et al. 2010). Outflowing gas is commonly traced via interstellar absorption lines blueshifted relative to stars and H II regions. It is found that a certain critical SFR surface density ($\sim 0.1 M_{\odot} \text{ yr}^{-1} \text{ kpc}^{-2}$) is necessary to drive an outflow (Murray et al. 2011; Kornei et al. 2012) and that outflows are stronger for

more massive and/or higher-SFR galaxies (Weiner et al. 2009; Kornei et al. 2012; Martin et al. 2012).

In order to study galactic outflows in *systematic* surveys at high redshifts ($z \gtrsim 1$), it is necessary to systematically select galaxies at targeted redshifts. The narrowband technique is one of the efficient methods used for this purpose, providing a systematic sample of galaxies with strong emission lines. The idea of this method is to use a narrowband filter to detect a specific nebular emission line redshifted into the narrow wavelength range of the filter. This method has provided vast numbers of star-forming galaxies ranging from low redshifts to redshifts as high as $z \sim 7.0$. At $z \leq 2.0$, star-forming galaxies with strong [O II], [O III], and H α emission lines are selected as [O II], [O III], and H α emitters, respectively (e.g., Bunker et al. 1995; Ly et al. 2012; Drake et al. 2013). Another important type of star-forming galaxy selected via this method is Lyman alpha emitters (LAEs), which show a strong Ly α emission line. Thousands of LAEs have been selected at various redshifts over $z \sim 0.3$ – 7.0 (e.g., Cowie et al. 2010; Ouchi et al. 2008, 2010).

Some LAEs show very luminous and extended (20–300 kpc) Ly α emission. They are called Ly α blobs (LABs; e.g., Matsuda et al. 2004) and are good candidates of galaxies with outflow at high redshifts. LABs are largely found at $z \sim 2$ – 3 with Ly α luminosities of $L(\text{Ly}\alpha) \gtrsim 10^{43} \text{ erg s}^{-1}$ and spatial extents over 50 kpc (Matsuda et al. 2004; Yang et al. 2009). The most remarkable LABs known at present are Steidel et al.’s (2000) LAB1 and LAB2 in SSA22 with $L(\text{Ly}\alpha) \simeq 10^{44} \text{ erg s}^{-1}$ and sizes of ~ 100 kpc. The most distant LAB is the one discovered by Ouchi et al. (2009) at $z \sim 7$; it shows $L(\text{Ly}\alpha)$ of $\sim 4 \times 10^{43} \text{ erg s}^{-1}$ and physically extends more than 17 kpc. Gas outflows by intense starbursts, black hole accretion (Mori et al. 2004; Taniguchi & Shioya 2000; Wilman et al. 2005), photoionization from massive stars, and/or AGNs (Matsuda et al. 2004; Geach et al. 2009) are plausible origins of LABs. However, we should note that inflows of cooling gas may also be able to produce LABs (Fardal et al. 2001; Smith & Jarvis 2007).

Recently, Brammer et al. (2013) reported an [O III] blob at $z = 1.61$ spatially extended over $1''$ or 8.5 kpc. The rest-frame equivalent width (EW_0) is $\sim 3500 \text{ \AA}$ for the blended H β and [O III] $\lambda\lambda 4959, 5007$ emission lines. This discovery was made by *Hubble Space Telescope* grism observations; therefore, they were able to resolve $1''$ extent beyond the galaxy, which would not be possible from the ground. Unlike resonantly scattered hydrogen-line emission such as Ly α emission that can be plausibly explained by both outflows and inflows, extended profiles of metal emission (i.e., oxygen-line emission) are more compatible with the outflow scenario rather than the inflow of pristine gas from the IGM whose metallicity is only $10^{-3} Z_{\odot}$ (e.g., Aguirre et al. 2008; Fumagalli et al. 2011).

To date, outflows from objects with oxygen-line emission have been studied only after the objects are identified as AGNs. In this paper, we use the narrowband technique to conduct the first systematic search for galaxies with outflow features at $z \simeq 1$, including both AGN host and star-forming galaxies. We look for [O II] emission instead of [O III] emission, because we aim to study galaxies as distant as possible and [O II] is the shortest-wavelength strong metal emission line. This systematic search enables us to provide a meaningful constraint on the frequency of outflow occurrence in star-forming galaxies at $z \gtrsim 1$, a crucial epoch that the star formation activity of massive galaxies is being quenched.

This paper is organized as follows. Section 2 describes the data and the selection method used to identify [O II] blobs (O II Bs). We also measure photometry and derive stellar properties of the selected O II Bs. Section 3 explains the photometric, stellar, and spectroscopic properties of a giant O II B we discover. Section 4 presents the spectroscopic data of other O II Bs. Section 5 discusses the AGN activity, the signature of an outflow, and its possible origins for this giant blob. We also estimate the number density of O II Bs. Finally, we summarize all results in Section 6.

Throughout this paper, magnitudes are described in the AB system. We assume a standard Λ CDM cosmology with parameters of $(\Omega_m, \Omega_{\Lambda}, H_0) = (0.3, 0.7, 70 \text{ km s}^{-1} \text{ Mpc}^{-1})$.

2. O II B CANDIDATES AT $z \sim 1.2$

2.1. Sample Selection

To search for O II Bs, we first select [O II] emitters whose [O II] emission falls into the narrowband filter *NB816* with $\lambda_c = 8150 \text{ \AA}$ and $\text{FWHM} = 120 \text{ \AA}$. We use the catalog of [O II] emitters at $z \sim 1.2$ provided by Drake et al. (2013). Full details in the selection of [O II] emitters are described in Drake et al. (2013); a brief description is as follows. An *NB816* image was taken with Subaru/Suprime-Cam for an area of $\sim 1 \text{ deg}^2$ in the Subaru-*XMM* Deep Survey (SXDS) field by Ouchi et al. (2008). Its 5σ limiting magnitude is 26.0 mag on a $2''.0$ diameter aperture. Deep broadband (*B*, *V*, *R*, *i*, and *z*) images were also obtained by Furusawa et al. (2008) whose 5σ limiting magnitudes on a $2''.0$ aperture are 27.39, 27.10, 26.85, 26.66, and 25.95 mag, respectively. To obtain good quality photometric redshifts, they also use *u*-band data from Megacam on the Canada–France–Hawaii Telescope (CFHT), *J*, *H*, *K* data from DR8 of the UKIDSS Ultra Deep Survey (UDS; Lawrence et al. 2007) taken with WFCAM on the UK Infrared Telescope (UKIRT), and Infrared Array Camera (IRAC) channels 1 ($3.6 \mu\text{m}$) and 2 ($4.5 \mu\text{m}$) from *Spitzer* UDS survey (SpUDS; PI: J. Dunlop). [O II] emitters are selected in a 0.62 deg^2 region (after masking) where the SXDS/UDS data overlap.

Object detection was made on the *NB816* image. Then, for all objects above the 5σ limiting magnitude, $2''.0$ diameter aperture magnitudes are measured for the other bandpasses at exactly the same positions as in the *NB816* image by using the dual mode of SExtractor (Bertin & Arnouts 1996). Emitter candidates are required to exhibit a significant excess in *NB816* with respect to an offband defined by a combination of the *R* and *z* bands (Figure 2 in Drake et al. 2013). Possible interlopers (i.e., late-type red stars) are removed from the emitter candidates by applying the *B*–*z* and *z*–*K* color diagram (Daddi et al. 2004) and *B*–*z* > 2.5 criterion. To summarize, Drake et al. (2013) have 3597 *NB816*-excess objects classified as galaxies. 1013 of them are classified as [O II] emitters at $0.80 < z < 1.50$ by using photometric redshifts, while the others are either H α emitters at $z \sim 0.25$ or [O III] emitters at $z \sim 0.63$.

To select O II Bs, we adopt a similar methodology to what was used to search for LABs at $z = 3.1$ by Matsuda et al. (2004). We search for O II Bs in the emission-line *NB816*_{corr} image, which is obtained by subtracting a continuum-emission image from the *NB816* image; the continuum-emission image is constructed from the *R* and *z* images at $Rz \equiv (R + 2z)/3$. Then, objects are detected in the *NB816*_{corr} smoothed with a Gaussian kernel with a FWHM of $1''.0$. We regard an object as being extended if it consists of ≥ 20 continuous pixels above the 2σ background surface brightness fluctuation ($28 \text{ mag arcsec}^{-2}$

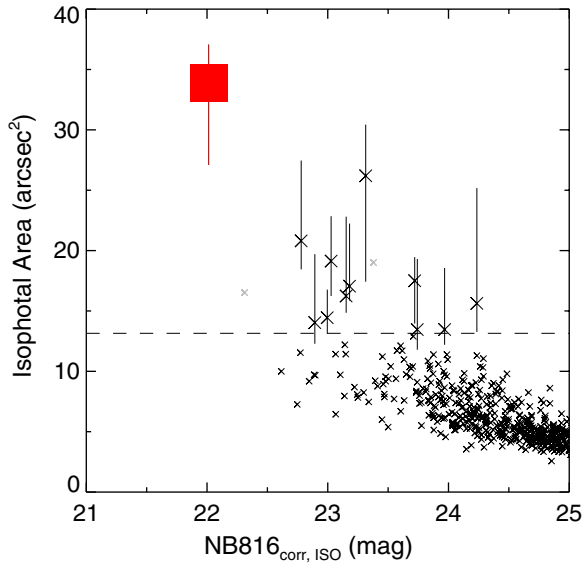


Figure 1. Distribution of isophotal area and magnitude on the $NB816_{\text{corr}}$ image for extended [O II] emitters at $z \sim 1.2$ (black crosses). The red square shows a giant O II B, O II B 1, and the large black crosses denote the small O II Bs. The gray crosses indicate two [O II] emitters that are not O II Bs, but objects with a large isophotal area made by source blending. The isophotal area criterion ($>13 \text{ arcsec}^2$) identical to that adopted by Matsuda et al. (2004) is shown with a horizontal dashed line. Fourteen emitters are above this criterion including O II B 1 and two objects with false detection. The error bars are defined by the 68% distributions of recovered isophotal areas given by our Monte Carlo simulations (see the text).

(A color version of this figure is available in the online journal.)

or $1.2 \times 10^{-18} \text{ erg s}^{-1} \text{ cm}^{-2} \text{ arcsec}^{-2}$) of the original $NB816_{\text{corr}}$ image. Extended objects are then crossmatched with the catalog of [O II] emitters described above. Figure 1 plots the isophotal area of extended [O II] emitters as a function of $NB816_{\text{corr}}$ magnitude. Matsuda et al. define their LABs as objects with an isophotal area above 16 arcsec^2 , corresponding to a spatial extent of 30 kpc at $z = 3.1$. By adopting the same criterion for our extended [O II] emitters, we find 14 objects to satisfy a criterion of isophotal area above 13 arcsec^2 (corresponding to a spatial

extent of 30 kpc at $z \sim 1.2$). We classify 12 of them as O II Bs after visual inspection. The remaining two objects are found to be blended with nearby objects in the smoothed $NB816_{\text{corr}}$ image, giving a falsely large isophotal area (the gray crosses in Figure 1). We estimate the uncertainties of isophotal area measurements by Monte Carlo simulations. We cut out images of the O II Bs, and place them on ~ 1000 empty sky regions of the $NB816_{\text{corr}}$ image to produce artificial O II B images. We measure their isophotal areas in the same manner as we performed for the real O II Bs, and define a 1σ error of isophotal area by the 68 percentile of the ~ 1000 artificial object distribution. The estimated uncertainties are presented in Figure 1.

We summarize properties of our 12 O II Bs at $z \sim 1.2$ in Table 1. O II Bs are called O II B 1 to 12 in order of isophotal area. Figure 2 shows $NB816$, $NB816_{\text{corr}}$, and Rz images of all 12 O II Bs. An isophote of 2σ -level surface brightness is overlaid on the Rz images, showing asymmetrically extended [O II] emission with relatively compact continuum emission.

2.2. Photometry and Stellar Properties

We perform photometry of our O II Bs with the 11 images of $uBVRIzJHK$ and IRAC 3.6 μm and 4.5 μm bands. Total magnitudes in the Subaru broadbands, $BVRiz$, are obtained from MAG_AUTO by SExtractor. Similarly, we measure MAG_AUTO magnitudes for the u -band image from Megacam on the CFHT and JHK images from DR10 of the UKIDSS UDS survey. For each image, we align the broadband images to the $NB816$ image and crossmatch the O II B positions after visual reconfirmation. IRAC and MIPS 24 μm imaging data were obtained from the SpUDS survey. For the IRAC images, total magnitudes are determined from aperture photometry on a $2''.4$ diameter aperture by applying aperture correction. The correction factor is calculated by generating artificial objects with given total magnitudes and recovering their aperture photometry.

We then derive the stellar properties, fitting model spectral energy distributions (SEDs) with the SEDs of 11 band photometry. The model SEDs are produced with the Bruzual & Charlot (2003) stellar population synthesis code. We assume a constant star formation history, the Salpeter (1955) initial mass

Table 1
Properties of 12 O II Bs at $z \sim 1.2$

ID	$NB816_{\text{corr}}$ ^a (mag)	$f([\text{O II}])^b$ ($\text{erg s}^{-1} \text{ cm}^{-2}$)	$L([\text{O II}])^c$ (erg s^{-1})	Area ^d (arcsec^{-2})	$\langle \text{SB} \rangle^e$ (mag arcsec^{-2})
O II B 1	22.01	3.1(−16)	2.5(+42)	34	25.8
O II B 2	23.31	9.3(−17)	7.5(+41)	26	26.9
O II B 3	22.78	1.5(−16)	1.2(+42)	21	26.1
O II B 4	23.03	1.2(−16)	9.7(+41)	19	26.2
O II B 5	23.72	6.4(−17)	5.1(+41)	18	26.8
O II B 6	23.18	1.1(−16)	8.4(+41)	17	26.3
O II B 7	23.15	1.1(−16)	8.7(+41)	16	26.2
O II B 8	24.23	4.0(−17)	3.2(+41)	16	27.2
O II B 9	23.00	1.2(−16)	1.0(+42)	14	25.9
O II B 10	22.89	1.4(−16)	1.1(+42)	14	25.8
O II B 11	23.74	6.3(−17)	5.0(+41)	13	26.6
O II B 12	23.97	5.1(−17)	4.1(+41)	13	26.8

Notes.

^a Isophotal magnitude in $NB816_{\text{corr}}$ images.

^b [O II] emission-line flux.

^c [O II] luminosity calculated by fixing redshifts at $z = 1.19$.

^d Isophotal area measured on the smoothed $NB816_{\text{corr}}$ image.

^e Average surface brightness.

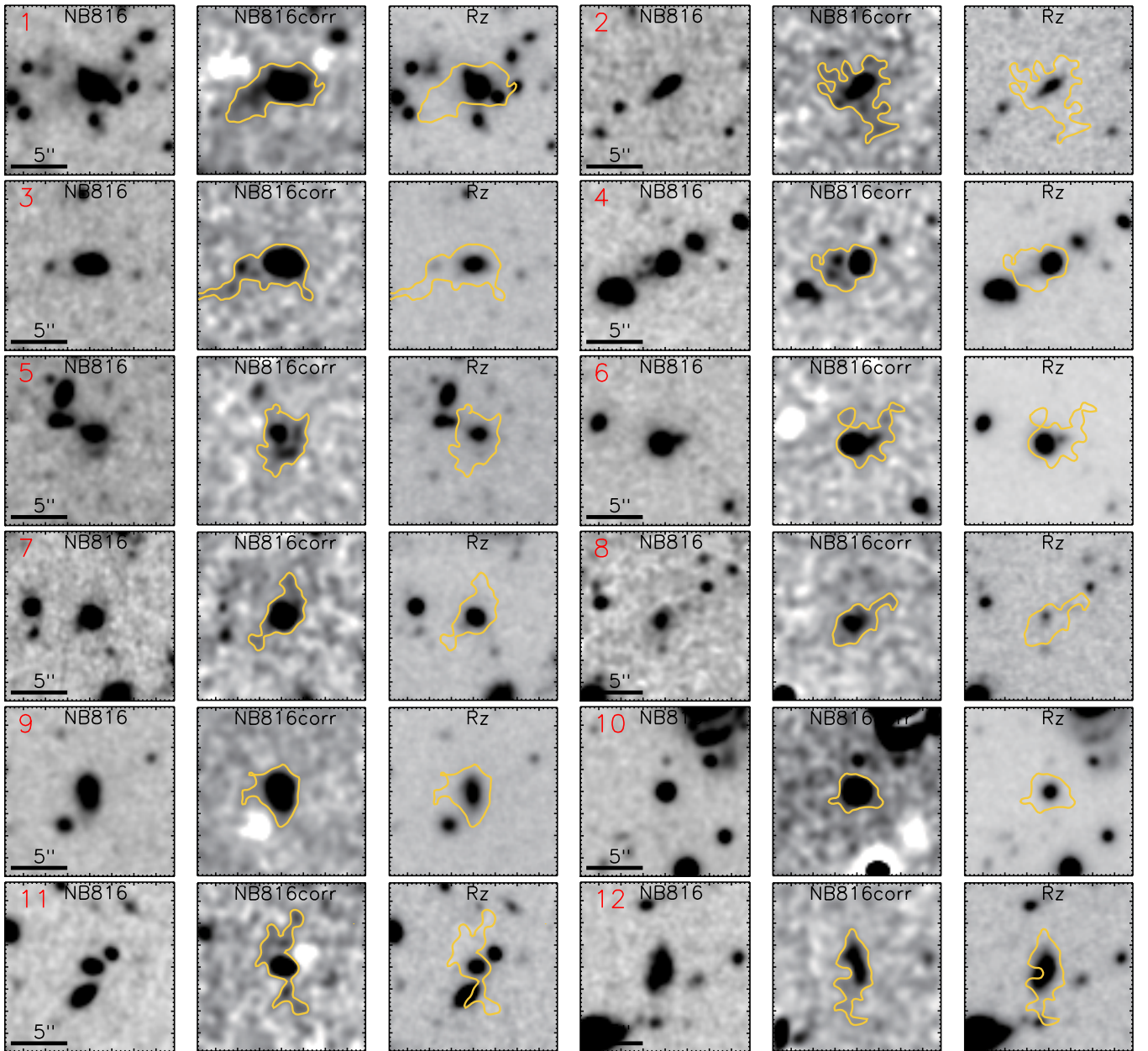


Figure 2. *NB816*, *NB816_{corr}*, and *Rz* images of 12 O II Bs. Images are arranged in order of isophotal area from left to right and top to bottom. O II B IDs are indicated at the top left corner of each *NB816* image. North is up and east is left. Each panel is $15'' \times 15''$ (corresponding to 124×124 kpc at $z = 1.19$) with the O II Bs at the center. The spatial scale is indicated in the *NB816* images. The yellow contours in the *Rz* images show the isophotal area above 2σ arcsec $^{-2}$ in the *NB816_{corr}* image as explained in Section 2.1.

(A color version of this figure is available in the online journal.)

function with standard lower and upper mass cutoffs of $0.1 M_{\odot}$ and $100 M_{\odot}$, respectively, dust attenuation law of Calzetti et al. (2000), and the solar metallicity. We fix the redshift to $z = 1.19$, assuming that the [O II] emission line falls in the center of *NB816* filter. We set a maximum stellar age of the O II Bs to ~ 5 Gyr, the cosmic age at $z = 1.19$.

We examine the star-forming nature of the O II Bs with a correlation between their stellar masses and SFRs derived from the SED fitting. It is known that star-forming galaxies at $z = 0-2$ have a tight stellar mass–SFR correlation referred to as a star formation main sequence (~ 0.2 dex scatter). The main sequence has a similar slope at any redshifts known to date, but the normalization of the main sequence decreases

from $z = 2$ to $z = 0$, which is related to the overall decline of cosmic SFR density (e.g., Daddi et al. 2007; Elbaz et al. 2007). Passive galaxies with high stellar masses are located far below the main sequence and they are regarded as progenitors of elliptical galaxies in the local universe. Figure 3 shows the stellar mass–SFR relation for all O II Bs at $z \sim 1.2$. In the low-mass regime, the O II Bs show a positive correlation between stellar mass and SFR. The distribution of O II Bs does not follow the main sequence, but presents a plateau at the high-mass end of $\gtrsim 10^{10} M_{\odot}$. The O II Bs fall below the main sequence at $> 10^{11} M_{\odot}$. Albeit with the small statistics, it would imply that low-mass O II Bs are actively star forming, while high-mass O II Bs quench their star formation. In Figure 3, O II B 1 is the

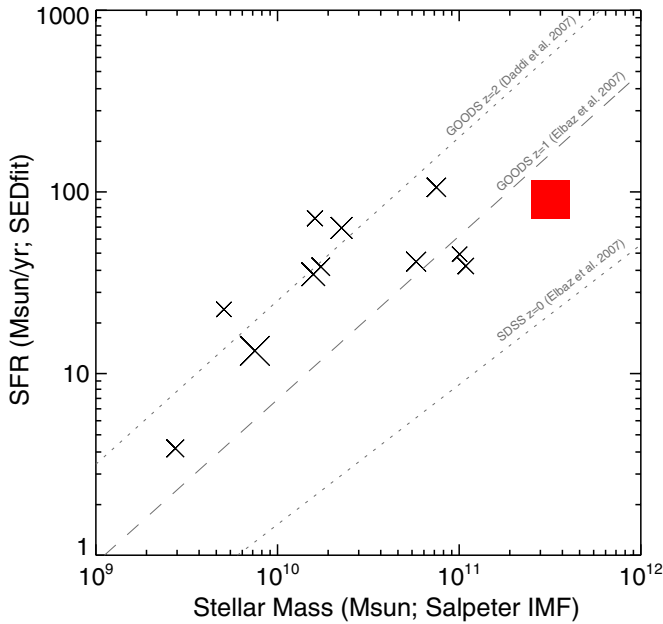


Figure 3. Stellar mass–SFR correlation for O II Bs at $z \sim 1.2$ in SXDS. The red solid square represent O II B 1, the most extended O II B, while black crosses indicate other smaller O II Bs. The size of the symbols is proportional to the isophotal area of the O II B each symbol represents. The dashed line is the $z = 1$ correlation taken from Elbaz et al. (2007). The dotted lines are the $z = 0$ and $z = 2$ correlations taken from Elbaz et al. (2007) and Daddi et al. (2007), respectively.

(A color version of this figure is available in the online journal.)

most massive blob and its SFR is below the main sequence, implying that it is quenching star-forming activity. Similarly, two other O II Bs, blobs 9 and 12 below the sequence, are probably quenching their star formation.

3. O II B 1 AT $z \sim 1.2$

Among 12 O II Bs at $z \sim 1.2$, O II B 1 (R.A. = $02^{\text{h}}17^{\text{m}}08^{\text{s}}.64$, decl. = $-04^{\circ}50'22''.88$) is the brightest emitter and shows the most extended profile in the $NB816_{\text{corr}}$ image (red square in Figure 1) with an isophotal area of 34 arcsec^2 . The rest-frame equivalent width and [O II] luminosity of O II B 1 are estimated from the $NB816$ and R_z images to be $71 \pm 10 \text{ \AA}$ and $3.2 \pm 0.2 \times 10^{42} \text{ erg s}^{-1}$, respectively. This luminosity is significantly brighter than the typical [O II] emitters found in the literature (e.g., Ly et al. 2012; Drake et al. 2013).

Being extended over $9''$ or $\sim 75 \text{ kpc}$ along the major axis, O II B 1 is remarkably larger than the [O III] blob at $z = 1.6$ reported by Brammer et al. (2013). However, a direct comparison is difficult due to the different sensitivity limits. Figure 4 presents the azimuthally averaged [O II] emission surface brightness profiles of O II B 1 measured with the $NB816_{\text{corr}}$ image. The red line in Figure 4 is the surface brightness of ellipsoidal isophote along the elongated direction, i.e., east–west direction, that is illustrated with the yellow isophote in Figure 2. The profile of ellipsoidal isophotes is extended to the radius of $\sim 3''.0$, $4''.1$, and $4''.3$ along the semi-major axis at the 5σ , 3σ , and 2σ surface brightness levels, respectively. This indicates that [O II] emission of O II B 1 is remarkably extended even at the 5σ surface brightness limit. For comparison, we show the surface brightness of circular isophotes with the gray dotted line in Figure 4. This surface brightness profile of circular isophote is truncated at the relatively small angular distance, because O II B 1 is highly elongated.

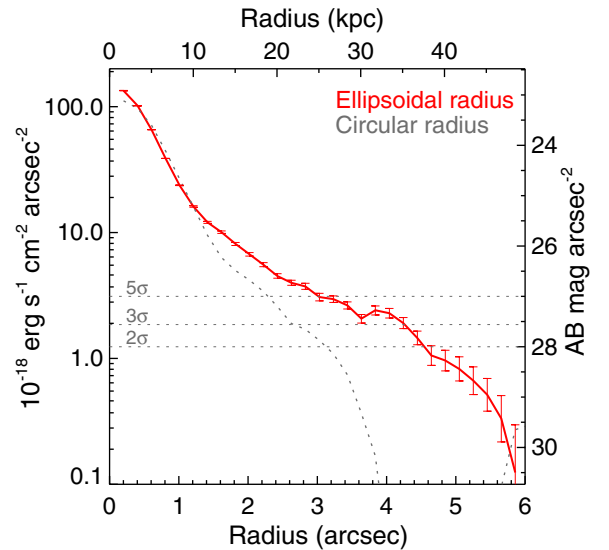


Figure 4. Azimuthally averaged [O II] surface brightness profiles of O II B 1. The red and gray lines are the [O II] profiles measured in the $NB816_{\text{corr}}$ image with the ellipsoidal radius (semi-major axis) and circular radius, respectively. Error bars represent the root-mean-square values around the average profile. Horizontal dotted lines indicate the surface brightness limits of the 5σ , 3σ , and 2σ levels, from top to bottom.

(A color version of this figure is available in the online journal.)

3.1. Photometric Properties

The photometry of O II B 1 in the 11 bands ($uBVRIzJHK$ and IRAC $3.6 \mu\text{m}$ and $4.5 \mu\text{m}$) is determined and given in Section 2.2. In addition to the 11 band photometry, we use the MIPS $24 \mu\text{m}$ flux of O II B 1, $298 \pm 7 \mu\text{Jy}$, which is carefully measured by Simpson et al. (2012). The X-ray photometry of O II B 1 is obtained from the *XMM-Newton* catalog by Ueda et al. (2008). The flux in $0.3\text{--}0.5 \text{ keV}$ is calculated by assuming the photon index of 1.5, while the index of 2.0 is assumed for $0.5\text{--}2.0 \text{ keV}$ and $2\text{--}10 \text{ keV}$ (Ueda et al. 2008). Finally, we take the radio 1.4 GHz flux from Simpson et al. (2012). The radio observation was carried out with the Very Large Array (VLA) of the National Radio Astronomy Observatory (Simpson et al. 2006), and the 1.4 GHz radio flux is $216 \pm 22 \mu\text{Jy}$. All of the measurements are listed in Table 2.

Stellar properties of O II B 1 are obtained in the same manner as those of the other O II Bs in Section 2.2, but with the spectroscopic redshift of $z = 1.18$ (see Section 3.2.2). The best-fit SED of O II B 1 has a very old stellar age, 4.7 Gyr , comparable with the cosmic age at $z = 1.18$. The stellar mass is $3.2 \times 10^{11} M_{\odot}$. The SFR is $90 M_{\odot} \text{ yr}^{-1}$ and the color excess $E(B - V)$ is 0.3 mag . Figure 5 presents the SED and the best-fit model of O II B 1.

3.2. Spectroscopic Properties

3.2.1. Observations

The spectroscopic observation of O II B 1 was carried out with the Visible Multi-Object Spectrograph (VIMOS) on the Very Large Telescope (VLT) as part of the European Southern Observatory (ESO) program P074.A-033 (Simpson et al. 2012). The observation was conducted in service mode using the MR-orange grating and the GG475 order-sorting filter, providing a spectral resolution of $\lambda/\Delta\lambda \simeq 580$ ($1''$ slit) and a spectral dispersion of $2.5 \text{ \AA pixel}^{-1}$ over the wavelength range of $4800\text{--}10000 \text{ \AA}$. The slit is located at the center of the blob in the

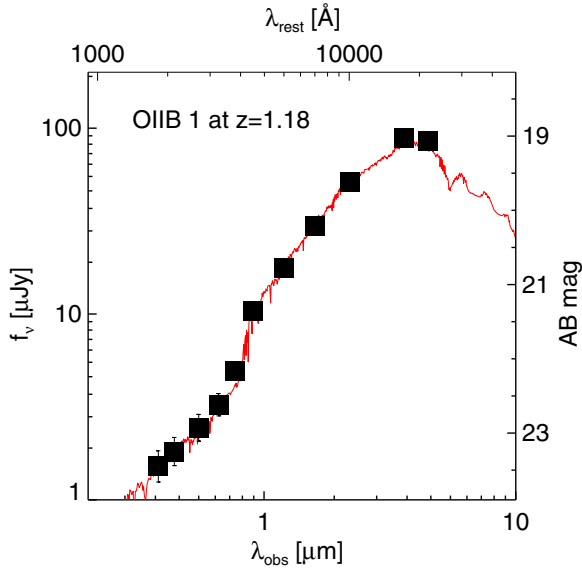


Figure 5. SED of O II B 1. The black squares show the total fluxes in 11 bands used in SED fitting (Table 2). The red line represents the best-fitting model described in Section 3.1.

(A color version of this figure is available in the online journal.)

Table 2
Photometry of O II B 1

Band	Total Magnitude/Flux
$f(0.3\text{--}0.5\text{ keV})^a$	$2.8 \pm 2.5 \times 10^{-16}$
$f(0.5\text{--}2.0\text{ keV; soft})^a$	$1.1 \pm 0.4 \times 10^{-15}$
$f(2\text{--}10\text{ keV; hard})^a$	$1.7 \pm 0.6 \times 10^{-14}$
u	23.45 ± 0.21
B	23.25 ± 0.19
V	22.93 ± 0.18
R	22.62 ± 0.15
$NB816$	19.78 ± 0.04
i	22.16 ± 0.12
z	21.36 ± 0.09
J	20.78 ± 0.06
H	20.22 ± 0.05
K	19.63 ± 0.04
$m(3.6\text{ }\mu\text{m})$	19.03 ± 0.05
$m(4.5\text{ }\mu\text{m})$	19.07 ± 0.05
$f(24\text{ }\mu\text{m})$	$298 \pm 7\text{ }\mu\text{Jy}$
$f(1.4\text{ GHz})$	$216 \pm 22\text{ }\mu\text{Jy}$

Note. ^a The X-ray fluxes are taken from Ueda et al. (2008) in units of $\text{erg s}^{-1} \text{cm}^{-2}$.

north–south direction as a default of VIMOS. The total exposure time was 5400 s. Data reduction is performed using the standard pipeline and described in detail in Simpson et al. (2012). The wavelength calibration has a root-mean-square (rms) uncertainty of 0.4 pixels or 1.0 Å. The estimated 3σ limiting flux for detecting an emission line is $\sim 10^{-17} \text{ erg s}^{-1} \text{cm}^{-2}$ over $5300 \text{ Å} \lesssim \lambda \lesssim 7700 \text{ Å}$ spectral range.

3.2.2. Emission-line Identification

Figure 6 shows the overall VIMOS spectrum of O II B 1 extracted through a $1''$ aperture with an enhanced spectrum at the wavelength around a remarkably strong emission line in the inset figure. A two-dimensional spectrum around the line is also shown in the top panel of the inset figure, where the south end of the slit is up. The central wavelength of this single line is

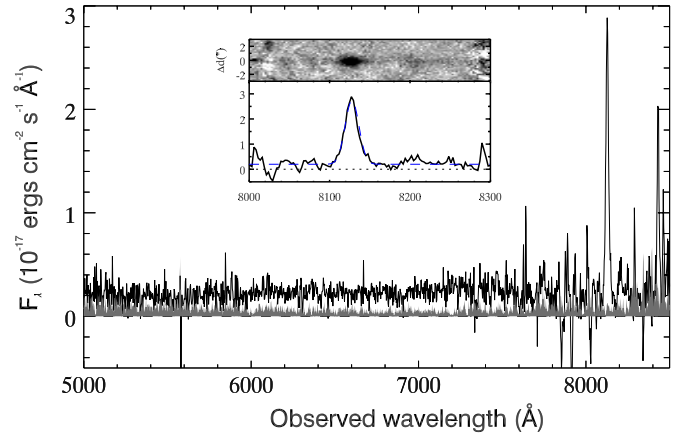


Figure 6. VIMOS spectrum of O II B 1 at $z = 1.18$ displayed in the observed frame. The solid line shows the observed spectrum and the gray shaded region indicates 1σ sky noise. The inset figure illustrates a close-up view of the spectrum around the strong emission line at 8127.9 Å with a two-dimensional spectrum on the top. The blue dashed line represents the best-fitting Gaussian profile.

(A color version of this figure is available in the online journal.)

8127.9 Å . We investigate whether this line is $\text{Ly}\alpha$, [O II], [O III], or $\text{H}\alpha$ emission. We exclude the possibility of $\text{H}\alpha$ emission at $z = 0.24$, as the spectrum shows no detection of [O III] $\lambda 5007$ emission at $\simeq 6209 \text{ Å}$ and [O II] $\lambda 3727$ emission at $\simeq 4621 \text{ Å}$. It is not [O III] at $z = 0.62$, either, because it lacks detection of [O III] $\lambda 4959$ emission at $\simeq 8034 \text{ Å}$ and [O II] $\lambda 3727$ emission at $\simeq 6038 \text{ Å}$. Furthermore, clear detection of continuum-emission blueward of this line indicates that this object is not a $\text{Ly}\alpha$ emitter at $z = 5.68$. Additionally, the derived photometric redshift quite strongly peaked around $z = 1.2$ (Drake et al. 2013). We thus conclude that this line is [O II] emission at $z = 1.1808$.

Because the VIMOS spectral resolution is only $R = 580$, the [O II] $\lambda\lambda 3726, 3729$ doublet is not resolved. We thus simply fit the [O II] emission line with a single symmetric Gaussian profile by using the IDL MPFITEXPR routine, which is part of the IDL MPFIT package (Markwardt 2009).⁶ We measure the line flux of O II B 1 to be $5.5 \pm 0.2 \times 10^{-16} \text{ erg s}^{-1} \text{cm}^{-2}$, corresponding to an [O II] luminosity of $4.3 \pm 0.2 \times 10^{42} \text{ erg s}^{-1}$. We summarize spectroscopic properties of O II B 1 in Table 3.

3.2.3. Spectral Properties of Other Lines

We also try to detect other emission or absorption lines falling into the wavelength range of the VIMOS spectrum: Fe II 2344, 2374, 2587, 2600, Fe II* 2613, 2626, 2632, Mg II 2796, 2804, and [Ne V] 3427. We fit all lines with a single Gaussian profile using the MPFIT package to determine the central wavelength, FWHM, and flux. Lines with no detection are shown in Figure 7, while those with a tentative signature are shown separately in Figure 8. Each line is plotted as a function of velocity offset with respect to the systemic velocity calculated from the [O II] emission line.

The top left panel of Figure 8 shows a very tentative Fe II $\lambda 2587$ absorption line with only 2.2σ at 5628.0 Å , corresponding to a line redshift of $z_{\text{line}} = 1.1764$. Likewise, we find marginal detection of the fine-structure Fe II* $\lambda 2613$ emission line at the 2.2σ significant level at 5690.6 Å or $z_{\text{line}} = 1.1772$ (top right panel of Figure 8). The bottom left panel shows 3σ marginal detection of Mg II $\lambda 2796$ emission

⁶ <http://www.physics.wisc.edu/~craigm/idl/>

Table 3
Properties of O II 1

Quantity	Value
Redshift (z)	1.1804 ± 0.0003 ^a
Isophotal area ^b in $NB816_{\text{corr}}$	34 arcsec^2
Major axis ^c in $NB816_{\text{corr}}$	$9''$ or 75 kpc
Half-light radius ^d in $NB816_{\text{corr}}$	$1''0$ or 8.3 kpc
$f([\text{O II}])^e$ (VIMOS)	$5.5 \pm 0.2 \times 10^{-16} \text{ erg s}^{-1} \text{ cm}^{-2}$
$L([\text{O II}])^e$ (VIMOS)	$4.3 \pm 0.2 \times 10^{42} \text{ erg s}^{-1}$
$f([\text{O II}])$ ($NB816$ and R_z images)	$1.9 \pm 0.3 \times 10^{-15} \text{ erg s}^{-1} \text{ cm}^{-2}$
$L([\text{O II}])$ ($NB816$ and R_z images)	$1.5 \pm 0.2 \times 10^{43} \text{ erg s}^{-1}$
M_B ^f	$-22.34 \pm 0.09 \text{ mag}$
$[\text{O II}] \text{ EW}_0$ ^g (VIMOS)	$126 \pm 14 \text{ \AA}$
$[\text{O II}] \text{ EW}_0$ (from $NB816$ and R_z)	$237^{+37}_{-33} \text{ \AA}$
Stellar mass	$(1.6\text{--}3.2) \times 10^{11} M_\odot$
Stellar age	$4.3\text{--}4.7 \text{ Gyr}$
Color excess ($E(B - V)$)	0.3 mag
SFR from UV ^h	$52 \pm 4 M_\odot \text{ yr}^{-1}$
SFR from SED fit	$37\text{--}90 M_\odot \text{ yr}^{-1}$
SFR from $[\text{O II}]^h$	$213 \pm 62 M_\odot \text{ yr}^{-1}$
Number density	$5.3 \times 10^{-6} \text{ Mpc}^{-3}$
O II 1 fraction	0.1%

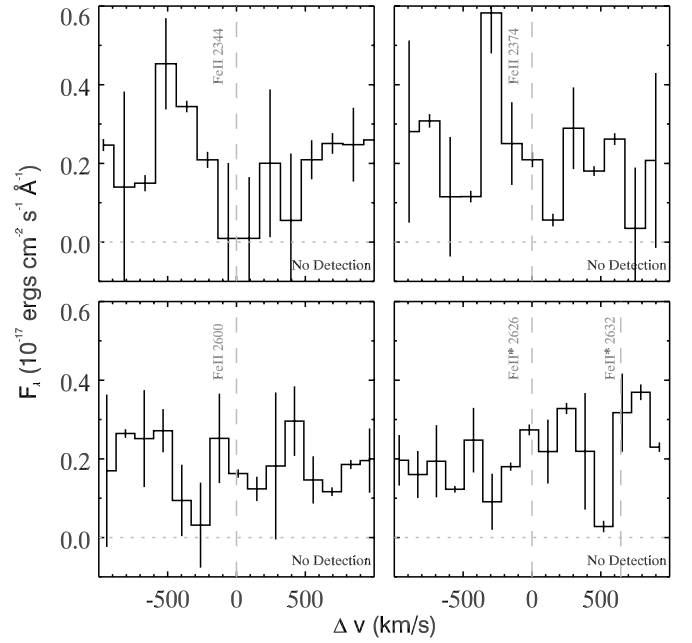
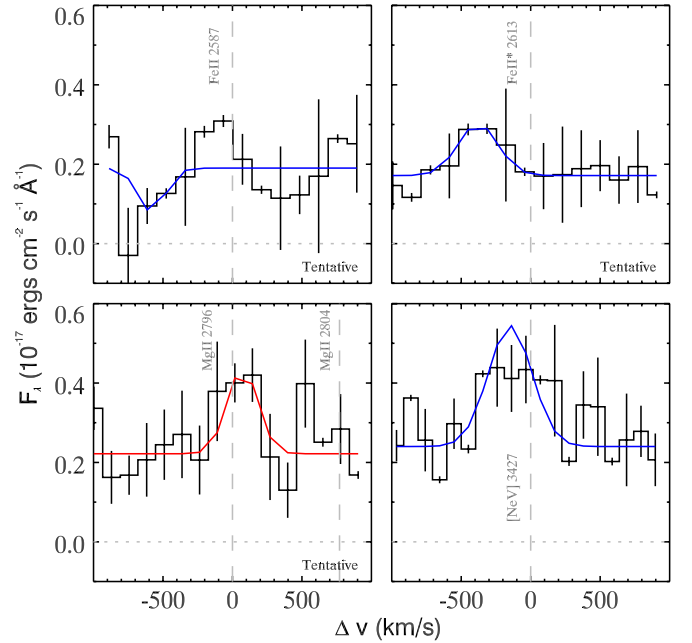
Notes.^a The spectroscopic redshift is obtained from cross-correlation between the target spectrum and a template spectrum as described in Simpson et al. (2012).^b The isophotal area is determined above $2\sigma \text{ arcsec}^{-2}$ ($28 \text{ mag arcsec}^{-2}$) in the $NB816_{\text{corr}}$.^c Major axis is determined in the smoothed $NB816_{\text{corr}}$ image by using the isophotal area shown in the SEGMENTATION image obtained from SExtractor.^d Half-light radius is a radius containing 50% of the total light from the object obtained by SExtractor.^e The VIMOS spectrum was obtained using $1''$ slit, which apparently do not cover the entire blob.^f The rest-frame B -band magnitude is calculated from the z -band photometry covering the rest-frame $3900\text{--}4500 \text{ \AA}$. It is close to bandpass of the B band; therefore, we do not apply k -correction to the magnitude.^g The rest-frame $[\text{O II}]$ equivalent width (EW_0) is calculated from the VIMOS spectrum covering only $1''$ at the center of the O II 1.^h The SFRs are derived, respectively, from the UV continuum and $[\text{O II}]$ luminosity by applying the relation from Kennicutt (1998) without any dust extinction.

line at 6097.5 \AA , whose redshift, $z_{\text{line}} = 1.1805$, is very close to the systemic redshift derived from the $[\text{O II}]$ emission line. The last line, $[\text{Ne V}] \lambda 3427$, is detected with a high significance level of 6σ at 7467.0 \AA , or $z_{\text{line}} = 1.1789$. Its flux is derived to be $2.5 \pm 1.6 \times 10^{-17} \text{ erg s}^{-1} \text{ cm}^{-2}$. The properties of these absorption and emission lines are summarized in Table 4.

4. O II 1 AND 8

4.1. Spectroscopic Data

In addition to the VIMOS spectrum of O II 1, we also have spectroscopic data for another two blobs, O II 4 and 8. The observations were carried out with the Faint Object Camera and Spectrograph (FOCAS) mounted on the Subaru Telescope. The spectrum of O II 4 was obtained with the 150 grism and an SY47 order-cut filter providing a spectral resolution of $\lambda/\Delta\lambda \simeq 250$ ($0''.8$ slit) over $4700\text{--}9400 \text{ \AA}$. The total exposure time was 3600 s. The spectrum of O II 8 was taken with the 300 blue grism and the SY47 order-cut filter with a spectral resolution of 500 ($0''.8$ slit). The total exposure time was 7200 s. Data reduction is performed with IRAF following the standard method for the optical multi-slit spectroscopy. The estimated

**Figure 7.** Spectra of non-detected Fe II and Fe II* lines of O II 1 as a function of velocity offset with respect to the systemic velocity (vertical dashed lines) calculated from the $[\text{O II}]$ emission. Error bars indicate 1σ sky uncertainty.**Figure 8.** Spectra of absorption and emission lines that are tentatively detected of O II 1 as a function of velocity offset with respect to the systemic velocity calculated from the $[\text{O II}]$ emission (vertical dashed lines). Error bars indicate 1σ sky uncertainty. Blue and red dashed lines represent the best-fitting Gaussian profiles of blueshifted and redshifted lines, respectively.

(A color version of this figure is available in the online journal.)

3σ limiting flux density are $2 \times 10^{-18} \text{ erg s}^{-1} \text{ cm}^{-2} \text{ \AA}^{-1}$ and $1 \times 10^{-18} \text{ erg s}^{-1} \text{ cm}^{-2} \text{ \AA}^{-1}$ over $5300 < \lambda < 7700 \text{ \AA}$ spectral range for spectra of O II 4 and 8, respectively.

4.2. Spectroscopic Properties

Figure 9 shows the FOCAS spectrum of O II 4 in the observed frame. There is a single emission line at 8181.6 \AA . Here, we examine if this line is $\text{Ly}\alpha$, $[\text{O II}]$, $[\text{O III}]$, or $\text{H}\alpha$

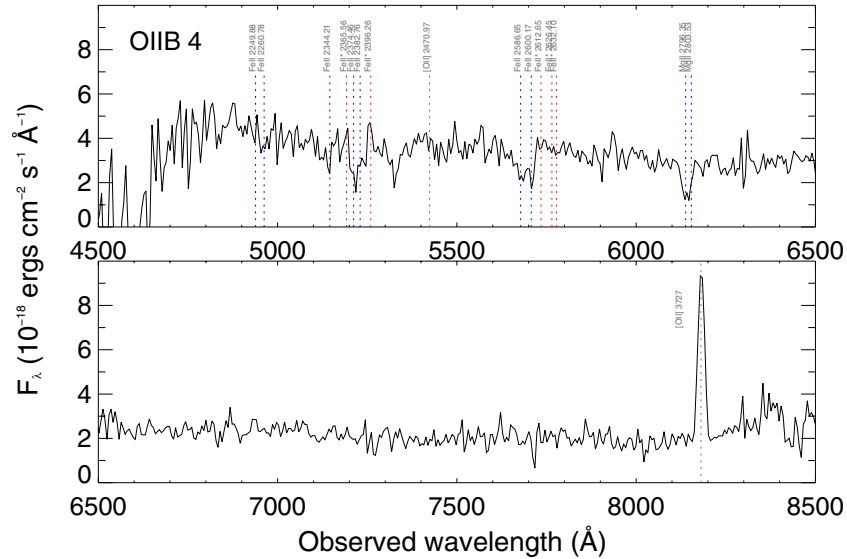


Figure 9. FOCAS spectrum of O II B 4 displayed in the observed frame. Red and blue vertical dotted lines indicate the expected emission and absorption lines, respectively, based on the systemic redshift determined with the [O II] emission line (black dotted line).

(A color version of this figure is available in the online journal.)

Table 4
Line Properties of O II B 1

Line (1)	λ_{rest} (Å) (2)	λ_{obs} (Å) ^a (3)	z_{line} (4)	Flux ^a (5)
Fe II ^b	2587	5628.0	1.1764	Absorption?
Fe II ^{*b}	2613	5690.6	1.1772	Emission?
Mg II ^b	2796	6097.5	1.1805	Emission?
[Ne v]	3427	7467.0 ± 4.1	1.1789 ± 0.0012	$2.5 \pm 1.6 \times 10^{-17}$
[O II]	3727	8127.9 ± 8.6	1.1808 ± 0.0023	$5.5 \pm 0.2 \times 10^{-16}$

Notes. Columns: (1)–(2) Line names and their rest-frame wavelengths. (3) Observed wavelengths of the lines obtained from best-fitting Gaussian profiles by MPFIT. (4) Redshifts. (5) Observed fluxes in the units of $\text{erg s}^{-1} \text{cm}^{-2}$.

^a An error on the observed wavelengths is a standard deviation obtained from fitting a line with a single Gaussian profile.

^b These lines are just marginally detected. Discussion using these lines should be done with caution.

emission. It is not H α emission at $z = 0.25$ because it lacks detection of [O III] $\lambda 5007$ line at 6242 Å and [O II] $\lambda 3727$ line at 4646 Å. We also rule out the possibility that this is an [O III] $\lambda 5007$ line at $z = 0.63$, because we do not find an [O III] $\lambda 4959$ line at 8103 Å or an [O II] $\lambda 3727$ line at 6090 Å. Likewise, the line is not Ly α emission at $z = 5.73$ as we certainly detect the continuum blueward of the line. We thus conclude that the single emission at 8181.6 Å is an [O II] $\lambda 3727$ line emitted at $z = 1.195$. We fit the [O II] emission line with a Gaussian profile by MPFIT. The best-fit line flux is $1.7 \times 10^{-16} \text{ erg s}^{-1} \text{cm}^{-2}$, corresponding to the [O II] luminosity of $1.4 \times 10^{42} \text{ erg s}^{-1}$. The spectrum of O II B 4 shows a possible Mg II $\lambda \lambda 2796, 2804$ doublet absorption in the FOCAS spectrum (Figure 9). The absorption is blueshifted from the systemic redshift determined from the [O II] emission line with an average velocity offset of $\Delta v \sim -200 \text{ km s}^{-1}$.

The spectrum of O II B 8 is presented in Figure 10. This spectrum is so noisy that we detect no continuum, but one emission line at 8346.9 Å. We rule out the possibility that this is [O III] $\lambda 5007$ emission of a source at $z = 0.67$, because we

detect neither [O III] $\lambda 4959$ line at 8267 Å nor [O II] $\lambda 3727$ at 6213 Å. Similarly, this line is not H α emission at $z = 0.27$, because it lacks detection of [O III] $\lambda 5007$ at 6370 Å and [O II] $\lambda 3727$ at 4733 Å. The line is not the Ly α emission at $z = 5.86$, due to the clear ($>5\sigma$) detections of continuum blueward of the line in the $uBVR$ images. Using the spectrum, we confirm that the single line of O II B 8 at 8346.9 Å is the [O II] $\lambda 3727$ emission at $z = 1.24$. We estimate the [O II] emission-line flux and luminosity to be $5.6 \times 10^{-17} \text{ erg s}^{-1} \text{cm}^{-2}$ and $4.9 \times 10^{41} \text{ erg s}^{-1}$, respectively, by our Gaussian profile fitting.

5. DISCUSSION

5.1. AGN Activity

In this section, we examine the AGN activity of O II B 1 from several aspects. As the first step, we classify O II B 1 as an AGN due to the presence of [Ne v] emission. We have detected [Ne v] emission line with a flux of $2.5 \pm 1.6 \times 10^{-17} \text{ erg s}^{-1} \text{cm}^{-2}$, while star-forming regions cannot provide enough energy to produce high-ionization lines such as [Ne v].

The nucleus of O II B 1 is found to be an obscured type-2 AGN. The prominent 4000 Å break seen in the observed SED (Figure 5) indicates that we are not seeing the AGN continuum directly and that stellar components dominate the observed SED. Moreover, as listed in Table 3, the measured equivalent width of O II B 1 is 71 ± 10 Å for the entire blob. It is much higher than the *mean* equivalent widths of typical quasars, which is ~ 10 Å (Miller et al. 1992) or more precisely 7.80 ± 0.30 Å for radio-loud quasars and 4.77 ± 0.06 Å for radio-quiet samples at $z < 1.6$ (Kalfountzou et al. 2012). Although quasar samples in Kalfountzou et al. (2012) show a very broad [O II] equivalent width distribution ranging from $\text{EW}([\text{O II}]) \sim 0.1$ Å to $\text{EW}([\text{O II}]) \sim 100$ Å, only a few of their quasars ($<1\%$) show an $\text{EW}([\text{O II}])$ as large as 100 Å. The $\text{EW}([\text{O II}])$ of O II B 1 is far above those of the majority of quasars.

photoionization by star formation/AGN, AGN-driven wind, and/or shock excitation.

We constrain the origin of the marginal Fe II* $\lambda 2613$ emission of O II B 1 by following the description by Erb et al. (2012). They use CLOUDY code version 08.00 (Ferland et al. 1998) to construct the photoionization models by adopting the Starburst99 ionization spectrum (Leitherer et al. 1999). Constant star formation and a metallicity of $\sim 0.6 Z_{\odot}$ are assumed. While Erb et al. (2012) calculate an electron density of 100 cm^{-3} from an observed ratio of [O II] $\lambda 3729$ /[O II] $\lambda 3726$, the [O II] doublet of O II B 1 is not resolved. Different values of the electron density lead to difference values in the ionization parameter U (the ratio of ionizing photon density to the hydrogen density) in the sense that a higher density lowers the ionization parameter. The models show that the ratio of [O II] to Fe II* lines decrease with increasing U (Figure 15 in Erb et al. 2012). In our case, the [O II] $\lambda 3727$ /Fe II* $\lambda 2613$ ratio is tentatively, 68 ± 26 . The low [O II]/Fe II* ratio of O II B 1 would imply a very high ionization parameter ($\log U > -1.0$). Although we have not corrected the line ratio for dust extinction, the implied ionization parameter would be even higher when taking the dust effect into account, as we expect to see more of a decrease in Fe II* lines relative to the [O II] line in the presence of dust. Lilly et al. (2003) have found the ionization parameter of galaxies at $0.47 < z < 0.92$ to be $-3.2 \lesssim \log U \lesssim -2.5$, which is remarkably lower than the ratio derived in this paper. It is thus unlikely that the Fe II* emission originates from photoionization in H II regions of O II B 1. However, as the detection of Fe II* emission is indeed marginal, the derived [O II]/Fe II* ratio is probably just a lower limit and the corresponding ionization parameter is subsequently lower than discussed here.

The outflow velocity is an important quantity for determining whether outflow is driven by SNe or AGN. Heckman et al. (2000) study outflows in 32 luminous infrared galaxies at $z \lesssim 0.1$ including galaxies whose luminosities are powered by starburst as well as some powered by AGNs. They have found outflow velocities up to $400\text{--}600 \text{ km s}^{-1}$. More recently, Rupke et al. (2005a) and Rupke & Veilleux (2013) study outflows from ULIRGs at various redshifts and conclude that the central outflow velocities of SNe-driven wind are on average $\sim -100 \text{ km s}^{-1}$, while those of AGN-powered galaxies are $-200\text{--}(-1500) \text{ km s}^{-1}$. As described in the previous section, the central velocity offsets of Fe II $\lambda 2587$ absorption line and Fe II* $\lambda 2613$ emission line for O II B 1 are $-605 \pm 99 \text{ km s}^{-1}$ and $-495 \pm 138 \text{ km s}^{-1}$, respectively. These central outflow velocities are generally comparable to those of AGN-powered galaxies. Thus, O II B 1 seems to favor the AGN-driven wind scenario that is thought to be one of the major effects of AGN feedback.

Shock excitation is another possible source powering large-scale outflow. Radiative shock can be formed at the interface of the fast-moving wind and a slow-moving ISM (Veilleux et al. 2005). Many studies found strong evidence of shock excitation dominating the emission (Veilleux & Rupke 2002; Veilleux et al. 2003; L  pari et al. 2004; Monreal-Ibero et al. 2010; Sharp & Bland-Hawthorn 2010; Rich et al. 2011). Shock can be distinguished from the others by examining various line ratios (e.g., [N II] $\lambda 6583$ /H α or [S II] $\lambda \lambda 6716, 6731$ /H α), which are not available in this study. Further spectroscopic observations, especially with an integral field unit spectrograph covering those lines, are necessary to determine whether the outflow of O II B 1 is powered by shock heating.

5.4. Can Gas Escape Out of the O II B 1?

We calculate the escape velocity inferred from the virial theorem using the simple equation of $V_{\text{esc}} \simeq \sqrt{2GM_{\text{halo}}/R}$, where M is the halo mass and R is the radius of the galaxy. The halo mass of O II B 1 is obtained from the derived stellar mass in Section 3.1 by applying the relationship between the stellar and halo masses given by Leauthaud et al. (2012). For the stellar mass of $3.2 \times 10^{11} M_{\odot}$, the halo mass ranges $1.0 \times 10^{13} M_{\odot}$. We define the radius of O II B 1 of $R_{\text{blob}} = 17.6 \text{ kpc}$ as twice the Petrosian radius $r(\eta = 0.2)$ measured in the Rz continuum image. The Petrosian radius is first introduced by Petrosian (1976) as the radius at which the surface brightness is η times the average surface brightness within this isophote. It is found that the magnitude within twice the Petrosian radius with $\eta = 0.2$ is approximately equal to the total magnitude for objects with exponential and Gaussian profiles and is $\sim 90\%$ of the total magnitude in the case of objects with $r^{1/4}$ profiles (Bershady et al. 2000).

The estimated escape velocity is 2208 km s^{-1} . This is larger than the velocity of the Fe II $\lambda 2587$ absorption and Fe II* $\lambda 2613$ emission lines ($495\text{--}605 \text{ km s}^{-1}$). If the detection of Fe II and Fe II* lines is real, it indicates that the majority of gas cannot escape out of the gravitational potential well of O II B 1 and cannot chemically enrich the IGM.

5.5. How Rare are O II Bs?

Drake et al. (2013) calculate the comoving volume of their [O II] emitter survey, corresponding to the FWHM of *NB816* times the survey area, to be $1.9 \times 10^5 \text{ Mpc}^3$. The number density of giant O II Bs like O II B 1 is thus $5.3 \times 10^{-6} \text{ Mpc}^{-3}$, whereas it is $6.3 \times 10^{-5} \text{ Mpc}^{-3}$ for all O II Bs (including O II B 1) selected by the same criterion as in Matsuda et al. (2004). The fraction of $z \sim 1.2$ [O II] emitters from Drake et al. that are blobs is 0.1% and 1.2% for giant O II B and small blobs, respectively.

Faber et al. (2007) study the evolution of the galaxy luminosity function up to $z \sim 1$ and propose a mixed scenario of star formation quenching, moving star-forming galaxies to the red sequence where they further merge with other small galaxies. They define blue and red galaxies according to the location on the $U - B$ versus M_B diagram and find the mean density of blue galaxies at $1 < z < 1.2$ to be $2.08 \times 10^{-3} \text{ Mpc}^{-3}$ down to $M_B \simeq -20.0 \text{ mag}$ in DEEP2 survey (Davis et al. 2003). To compare with this result, we estimate the rest-frame $U - B$ color from the observed $R - z$ color. The relationship between the $U - B$ and $R - z$ colors is determined using models with constant star formation history from Bruzual & Charlot (2003). All but one O II B at $z \sim 1.2$ is located in the blue cloud region of the color-magnitude diagram. Down to the same UV limit, we calculate the number density of O II Bs at $z \sim 1.2$ to be $6.3 \times 10^{-5} \text{ Mpc}^{-3}$. It implies that $\sim 3\%$ of blue galaxies at $1.0 \lesssim z \lesssim 1.2$ are quenching star formation by the same process as for our O II Bs.

As O II B 1 at $z = 1.18$ is classified as an obscured type-2 AGN (Section 5.1), it is important to compare the estimated number density with those of AGNs at similar redshifts. The number density of AGNs at $z \sim 1.0$ with hard X-ray luminosities of $L_{2\text{--}8 \text{ keV}} = 10^{44}\text{--}10^{45} \text{ erg s}^{-1}$ is $\sim 10^{-5} \text{ Mpc}^{-3}$ (Barger et al. 2005; Barger & Cowie 2005). An overall fraction of AGNs displaying outflows is approximately 60% (e.g., Ganguly & Brotherton 2008), albeit some variety depending on AGN properties. Consequently, the number density of AGNs with outflows at $z \sim 1.0$ is roughly $5.4 \times 10^{-6} \text{ Mpc}^{-3}$, which

is in good agreement with the number density of giant blobs like O II B 1. It is likely that the outflows from O II B 1 can be explained solely by AGN. However, the number density of all 12 O II Bs is larger than those of AGNs with outflows, implying that not all O II Bs are powered by AGNs. Additional observations are desirable to understand the nature of the entire population of O II Bs.

Since there is no systematic study of O II Bs up to date, it is difficult to state whether O II B 1 is a rare object or not. As a baseline of discussion, we compare the above number density to those corresponding to extended LABs at various redshifts. Studies of LABs at $z \sim 2.3$ (Yang et al. 2009) and at $z \sim 3$ (Matsuda et al. 2004; Saito et al. 2006) have determined their number densities of $3 \times 10^{-6} \text{ Mpc}^{-3}$, $3 \times 10^{-4} \text{ Mpc}^{-3}$, and $1 \times 10^{-5} \text{ Mpc}^{-3}$, respectively. At higher redshift, Ouchi et al. (2009) discovered an extended Ly α emitter at $z \sim 6.6$ and calculate the number density of LAB to be $1.2 \times 10^{-6} \text{ Mpc}^{-3}$. The number density of O II B 1-type objects is at least an order of magnitude smaller than those of LABs at $z \sim 3$ by Matsuda et al. (2004) and Saito et al. (2006), but comparable to the number densities of LABs at $z \sim 2.3$ by Yang et al. (2009) and at $z \sim 6.6$ by Ouchi et al. (2009). On the other hand, the number density of LABs at $z \sim 3$ is comparable to our study if it is compared with the number density of the entire O II B samples. Given that LAB surveys have shown that constraining the number density of the extended sources is challenging because of the intrinsic clustering or the selection criteria, we stress that the larger survey for O II Bs is required to further constrain their clustering and number density.

5.6. Diffuse [O II] Halos

Steidel et al. (2011) and Matsuda et al. (2012) have identified the diffuse, extended Ly α emission down to a very faint surface brightness limit in the composite images of UV-selected galaxies and/or LAEs at $z \sim 3$. The diffuse Ly α emission is thought to be a generic property of star-forming galaxies at high redshifts. Steidel et al. (2011) argue that Ly α emission of diffuse halos are produced by the resonance scattering of neutral H I gas in the circumgalactic medium (CGM).

In this section, we investigate whether extended [O II] emission is universally found in any [O II] emitters, using [O II] emission image ($NB816_{\text{corr}}$) composites. Figure 11 presents the stacked [O II] profiles for all O II Bs (the green line) and [O II] emitters (the blue line). We compare these surface brightness profiles with the one of O II B 1. Similar to O II B 1, the stacked image of the O II Bs shows an extended component at the radius larger than $1''$ over the point-spread function (PSF). On the other hand, the stacked profile of the all [O II] emitters of Drake et al. (2013) is similar to that of point sources (stars). We conclude that the extended nature of [O II] emission is not a common feature of star-forming galaxies. Unlike Ly α emission, [O II] emission is not resonantly scattered by H I gas in the CGM. Thus, the [O II] halos can probably be found only in high- z galaxies with strong outflows.

6. SUMMARY

We present the first systematic search for galaxies with spatially extended metal-line [O II] $\lambda\lambda 3726, 3729$ emission at $z \sim 1.2$, which we call “O II Bs.” We have discovered a giant blob with a spectroscopic redshift of $z = 1.18$, O II B 1. We have also discovered 12 small O II Bs. The O II B 1 extends over 75 kpc above $28 \text{ mag arcsec}^{-2}$ along its major axis. The rest-

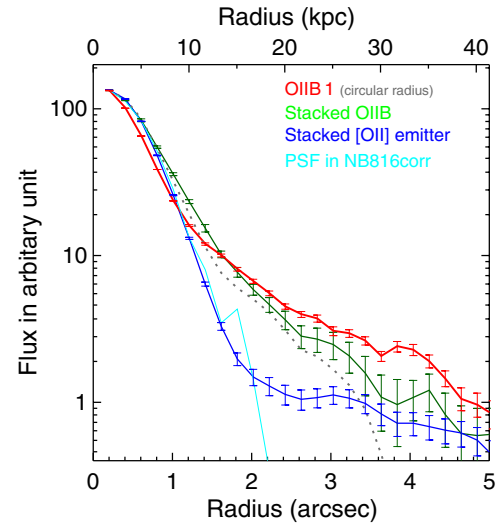


Figure 11. Surface brightness profiles of [O II] emission. The green solid line denotes the stacked [O II] profile of all 12 O II Bs including O II B 1, whereas the blue line is the stacked profile of all $z = 1.2$ [O II] emitters of Drake et al. (2013). The red solid and gray dotted lines represent the O II B 1 surface profiles of ellipsoidal and circular isophotes, which are the same as those presented in Figure 4. These surface brightness profiles are normalized at the innermost radius bin. Errors of the stacked profiles are estimated by Monte Carlo simulations that produce a large number of sky image composites in the same manner as the images for the stacked profiles. The surface brightness errors of O II B 1 are the same as those of Figure 4, which are rms values of surface brightness at the given radius bin. As a reference, the PSF profile is also shown.

(A color version of this figure is available in the online journal.)

frame equivalent width (EW_0) of the entire blob calculated from the $NB816$ and Rz images is $237^{+37}_{-33} \text{ \AA}$ and the [O II] luminosity is $1.5 \pm 0.2 \times 10^{43} \text{ erg s}^{-1}$. The major results of our study are summarized as follows.

1. A strong emission line has been detected at 8127.9 \AA in the VIMOS spectrum. We conclude that it is the [O II] emission at $z = 1.18$, because we do not find other strong emission lines at the bluer wavelengths which are expected if the line is H α at $z = 0.24$ or [O III] at $z = 0.62$, because we detect continuum-emission blueward of the line which is not expected if the line is Ly α at $z = 5.68$, and because the probability distribution of its photometric redshifts is peaked around $z = 1.2$.
2. We classify O II B 1 as a radio-quiet obscured type-2 AGN according to the following properties. (1) Mg II $\lambda 2796$ and [Ne V] $\lambda 3427$ emission lines are marginally detected in the VIMOS spectrum. (2) [O II] line width of $537 \pm 4 \text{ km s}^{-1}$ is larger than those observed for normal star-forming galaxies but smaller than those for typical broad-line AGNs. (3) A much higher [O II] equivalent width than typical AGNs and a prominent 4000 \AA break indicate that the AGN continuum is largely obscured. (4) The ratio of mid-infrared to radio fluxes ($q_{24} = 0.624$) is consistent with those for radio-quiet galaxies.
3. The outflow signature of O II B 1 is supported by the marginal existence of both Fe II $\lambda 2587$ absorption and Fe II* $\lambda 2613$ emission lines. Despite marginal detections, both lines show the consistent velocity offsets from the systemic velocity ($-605 \pm 99 \text{ km s}^{-1}$ and $-495 \pm 138 \text{ km s}^{-1}$ for Fe II $\lambda 2587$ and Fe II* $\lambda 2613$ lines, respectively).
4. Investigating the physical origins of the spatially extended [O II] emission and outflow, we have found that O II B 1 appears to favor the AGN-driven outflow scenario, though

shock excitation and photoionization by AGN cannot be ruled out. Photoionization by star formation is unlikely, because the ionization parameter inferred from the $[\text{O II}]/\text{Fe II}^*$ ratio of $\log U > -1.0$ is higher than the average values found in star-forming galaxies at similar redshifts. The AGN-driven wind is, in contrast, supported by the *central* outflow velocities derived from the $\text{Fe II } \lambda 2587$ absorption and $\text{Fe II}^* \lambda 2613$ emission lines, which are larger than those found in normal galaxies without an AGN, though the detection is tentative.

5. At $z \sim 1.2$, the number density of giant O II Bs like O II B 1 is $5.3 \times 10^{-6} \text{ Mpc}^{-3}$, while it is $6.3 \times 10^{-5} \text{ Mpc}^{-3}$ for the entire O II B sample. We estimate that approximately 3% of blue galaxies at $1.0 \leq z \leq 1.2$ may be experiencing star formation quenching process similar to the O II Bs. Comparing the number densities of the O II Bs with those of AGNs with outflow features at similar redshifts, we find that O II B 1 seems to be explained by AGN, but it is unlikely for the other O II Bs.

We thank the anonymous referee for careful reading and valuable comments that improved clarity of the paper. We are also grateful to Masao Hayashi, Shota Kisaka, Tomoki Saito, and Wiphu Rujopakarn for their useful comments and discussions. This work was supported by KAKENHI (23244025) Grant-in-Aid for Scientific Research (A) through Japan Society for the Promotion of Science (JSPS). S.Y. acknowledges support from the JSPS through JSPS postdoctoral fellowship for foreign researchers. C.S. and A.B.D. acknowledge support from the UK Science and Technology Facilities Council.

REFERENCES

- Aguirre, A., Dow-Hygelund, C., Schaye, J., & Theuns, T. 2008, *ApJ*, **689**, 851
- Alexander, D. M., Swinbank, A. M., Smail, I., McDermid, R., & Nesvadba, N. P. H. 2010, *MNRAS*, **402**, 2211
- Barger, A. J., & Cowie, L. L. 2005, *ApJ*, **635**, 115
- Barger, A. J., Cowie, L. L., Mushotzky, R. F., et al. 2005, *AJ*, **129**, 578
- Barnes, J. E., & Hernquist, L. 1992, *ARA&A*, **30**, 705
- Bershady, M. A., Jangren, A., & Conselice, C. J. 2000, *AJ*, **119**, 2645
- Bertin, E., & Arnouts, S. 1996, *A&AS*, **117**, 393
- Bradshaw, E. J., Almaini, O., Hartley, W. G., et al. 2013, *MNRAS*, **433**, 194
- Brammer, G. B., van Dokkum, P. G., Illingworth, G. D., et al. 2013, *ApJL*, **765**, L2
- Bruzual, G., & Charlot, S. 2003, *MNRAS*, **344**, 1000
- Bunker, A. J., Warren, S. J., Hewett, P. C., & Clements, D. L. 1995, *MNRAS*, **273**, 513
- Calzetti, D., Armus, L., Bohlin, R. C., et al. 2000, *ApJ*, **533**, 682
- Coil, A. L., Weiner, B. J., Holz, D. E., et al. 2011, *ApJ*, **743**, 46
- Cole, S., Lacey, C. G., Baugh, C. M., & Frenk, C. S. 2000, *MNRAS*, **319**, 168
- Cowie, L. L., Barger, A. J., & Hu, E. M. 2010, *ApJ*, **711**, 928
- Daddi, E., Cimatti, A., Renzini, A., et al. 2004, *ApJ*, **617**, 746
- Daddi, E., Dickinson, M., Morrison, G., et al. 2007, *ApJ*, **670**, 156
- Davis, M., Faber, S. M., Newman, J., et al. 2003, *Proc. SPIE*, **4834**, 161
- Dekel, A., Sari, R., & Ceverino, D. 2009, *ApJ*, **703**, 785
- Dekel, A., & Silk, J. 1986, *ApJ*, **303**, 39
- Drake, A. B., Simpson, C., Collins, C. A., et al. 2013, *MNRAS*, **433**, 796
- Elbaz, D., Daddi, E., Le Borgne, D., et al. 2007, *A&A*, **468**, 33
- Erb, D. K., Quider, A. M., Henry, A. L., & Martin, C. L. 2012, *ApJ*, **759**, 26
- Faber, S. M., Willmer, C. N. A., Wolf, C., et al. 2007, *ApJ*, **665**, 265
- Fardal, M. A., Katz, N., Gardner, J. P., et al. 2001, *ApJ*, **562**, 605
- Ferland, G. J., Korista, K. T., Verner, D. A., et al. 1998, *PASP*, **110**, 761
- Fumagalli, M., O'Meara, J. M., & Prochaska, J. X. 2011, *Sci*, **334**, 1245
- Furusawa, H., Kosugi, G., Akiyama, M., et al. 2008, *ApJS*, **176**, 1
- Ganguly, R., & Brotherton, M. S. 2008, *ApJ*, **672**, 102
- Geach, J. E., Alexander, D. M., Lehmer, B. D., et al. 2009, *ApJ*, **700**, 1
- Heckman, T. M., Armus, L., & Miley, G. K. 1990, *ApJS*, **74**, 833
- Heckman, T. M., Lehnert, M. D., Strickland, D. K., & Armus, L. 2000, *ApJS*, **129**, 493
- Ibar, E., Cirasuolo, M., Ivison, R., et al. 2008, *MNRAS*, **386**, 953
- Kalfountzou, E., Jarvis, M. J., Bonfield, D. G., & Hardcastle, M. J. 2012, *MNRAS*, **427**, 2401
- Kennicutt, R. C., Jr. 1998, *ARA&A*, **36**, 189
- Kereš, D., Katz, N., Davé, R., Fardal, M., & Weinberg, D. H. 2009, *MNRAS*, **396**, 2332
- Kornei, K. A., Shapley, A. E., Martin, C. L., et al. 2012, *ApJ*, **758**, 135
- Lawrence, A., Warren, S. J., Almaini, O., et al. 2007, *MNRAS*, **379**, 1599
- Leauthaud, A., Tinker, J., Bundy, K., et al. 2012, *ApJ*, **744**, 159
- Leitherer, C., Schaerer, D., Goldader, J. D., et al. 1999, *ApJS*, **123**, 3
- Lilly, S. J., Carollo, C. M., & Stockton, A. N. 2003, *ApJ*, **597**, 730
- Lípari, S., Mediavilla, E., García-Lorenzo, B., et al. 2004, *MNRAS*, **355**, 641
- Liu, G., Zakamska, N. L., Greene, J. E., Nesvadba, N. P. H., & Liu, X. 2013, *MNRAS*, **430**, 2327
- Ly, C., Malkan, M. A., Kashikawa, N., et al. 2012, *ApJ*, **757**, 63
- Markwardt, C. B. 2009, in ASP Conf. Ser. 411, *Astronomical Data Analysis Software and Systems XVIII*, ed. D. A. Bohlender, D. Durand, & P. Dowler (San Francisco, CA: ASP), **251**
- Martin, C. L. 2005, *ApJ*, **621**, 227
- Martin, C. L., Shapley, A. E., Coil, A. L., et al. 2012, *ApJ*, **760**, 127
- Matsuda, Y., Yamada, T., Hayashino, T., et al. 2004, *AJ*, **128**, 569
- Matsuda, Y., Yamada, T., Hayashino, T., et al. 2012, *MNRAS*, **425**, 878
- McIntosh, D. H., Bell, E. F., Rix, H.-W., et al. 2005, *ApJ*, **632**, 191
- Miller, P., Rawlings, S., Saunders, R., & Eales, S. 1992, *MNRAS*, **254**, 93
- Monreal-Ibero, A., Arribas, S., Colina, L., et al. 2010, *A&A*, **517**, A28
- Mori, M., Umemura, M., & Ferrara, A. 2004, *ApJL*, **613**, L97
- Murray, N., Ménard, B., & Thompson, T. A. 2011, *ApJ*, **735**, 66
- Murray, N., Quataert, E., & Thompson, T. A. 2005, *ApJ*, **618**, 569
- Naab, T., & Trujillo, I. 2006, *MNRAS*, **369**, 625
- Nesvadba, N. P. H., Lehnert, M. D., De Breuck, C., Gilbert, A. M., & van Breugel, W. 2008, *A&A*, **491**, 407
- Ouchi, M., Ono, Y., Egami, E., et al. 2009, *ApJ*, **696**, 1164
- Ouchi, M., Shimasaku, K., Akiyama, M., et al. 2008, *ApJS*, **176**, 301
- Ouchi, M., Shimasaku, K., Furusawa, H., et al. 2010, *ApJ*, **723**, 869
- Petrosian, V. 1976, *ApJL*, **209**, L1
- Prochaska, J. X., Kasen, D., & Rubin, K. 2011, *ApJ*, **734**, 24
- Rich, J. A., Kewley, L. J., & Dopita, M. A. 2011, *ApJ*, **734**, 87
- Rubin, K. H. R., Prochaska, J. X., Ménard, B., et al. 2011, *ApJ*, **728**, 55
- Rupke, D. S. N., & Veilleux, S. 2013, *ApJ*, **768**, 75
- Rupke, D. S., Veilleux, S., & Sanders, D. B. 2005a, *ApJS*, **160**, 87
- Rupke, D. S., Veilleux, S., & Sanders, D. B. 2005b, *ApJS*, **160**, 115
- Saito, T., Shimasaku, K., Okamura, S., et al. 2006, *ApJ*, **648**, 54
- Salpeter, E. E. 1955, *ApJ*, **121**, 161
- Shapley, A. E., Steidel, C. C., Pettini, M., & Adelberger, K. L. 2003, *ApJ*, **588**, 65
- Sharp, R. G., & Bland-Hawthorn, J. 2010, *ApJ*, **711**, 818
- Simpson, C., Martínez-Sansigre, A., Rawlings, S., et al. 2006, *MNRAS*, **372**, 741
- Simpson, C., Rawlings, S., Ivison, R., et al. 2012, *MNRAS*, **421**, 3060
- Smith, D. J. B., & Jarvis, M. J. 2007, *MNRAS*, **378**, L49
- Somerville, R. S., Hopkins, P. F., Cox, T. J., Robertson, B. E., & Hernquist, L. 2008, *MNRAS*, **391**, 481
- Soto, K. T., Martin, C. L., Prescott, M. K. M., & Armus, L. 2012, *ApJ*, **757**, 86
- Springel, V., & Hernquist, L. 2003, *MNRAS*, **339**, 312
- Steidel, C. C., Adelberger, K. L., Shapley, A. E., et al. 2000, *ApJ*, **532**, 170
- Steidel, C. C., Bogosavljević, M., Shapley, A. E., et al. 2011, *ApJ*, **736**, 160
- Steidel, C. C., Erb, D. K., Shapley, A. E., et al. 2010, *ApJ*, **717**, 289
- Taniguchi, Y., & Shioya, Y. 2000, *ApJL*, **532**, L13
- Toomre, A. 1977, *ARA&A*, **15**, 437
- Tremonti, C. A., Heckman, T. M., Kauffmann, G., et al. 2004, *ApJ*, **613**, 898
- Trujillo, I., & Aguerrí, J. A. L. 2004, *MNRAS*, **355**, 82
- Ueda, Y., Watson, M. G., Stewart, I. M., et al. 2008, *ApJS*, **179**, 124
- Veilleux, S., Cecil, G., & Bland-Hawthorn, J. 2005, *ARA&A*, **43**, 769
- Veilleux, S., & Rupke, D. S. 2002, *ApJL*, **565**, L63
- Veilleux, S., Shopbell, P. L., Rupke, D. S., Bland-Hawthorn, J., & Cecil, G. 2003, *AJ*, **126**, 2185
- Weiner, B. J., Coil, A. L., Prochaska, J. X., et al. 2009, *ApJ*, **692**, 187
- Wilman, R. J., Gerssen, J., Bower, R. G., et al. 2005, *Natur*, **436**, 227
- Yang, Y., Zabludoff, A., Tremonti, C., Eisenstein, D., & Davé, R. 2009, *ApJ*, **693**, 1579